Remote Sensing of Environment 245 (2020) 111825

Contents lists available at ScienceDirect

Remote Sensing of Environment

journal homepage: www.elsevier.com/locate/rse

Analysis of scattering characteristics from inland bodies of water observed by CYGNSS

Eric Loria[a,*], Andrew O'Brien[a], Valery Zavorotny[b], Brandi Downs[a], Cinzia Zuffada[c]

[a] Ohio State University, Columbus, OH, USA
[b] CIRES, University of Colorado Boulder, Boulder, CO, USA
[c] Jet Propulsion Laboratory, California Institute of Technology, Pasadena, CA, USA

ARTICLE INFO

Editor by Marie Weiss

Keywords:
GNSS Reflectometry
CYGNSS
Wetlands
Flooding
Bistatic radar

ABSTRACT

Measurements made by spaceborne Global Navigation Satellite System Reflectometry (GNSS-R) instruments have shown strong reflected power over inland waters that has been attributed to coherent scattering coming from the first Fresnel zone. Previous work in the field has shown the ability of GNSS-R to observe the global surface water distribution by generating dynamic maps of wetlands and other inundated areas. These maps can be generated by leveraging the large difference in received power of the GNSS signals as they reflect from water surfaces compared to land. In this paper, we utilize a full-forward scattering model approach to evaluate the accuracy of these maps. The CYGNSS End-to-End Simulator (E2ES) was extended to include the contributions from coherent surface scattering in heterogeneous regions where the area around the specular point contains both water and land in complex geometries. The simulator is then used to analyze the accuracy of a current approach to estimate the surface water content in the first Fresnel zone from a single measurement, called a fractional water in footprint approach. We find that contributions to the total received power by the scattering from outside the first Fresnel zone as well as CYGNSS instrument effects impact the accuracy of this approach. Furthermore, the measured signal from calibration scattering targets is compared to the results of simulation to validate the scattering model. The work shows that the variability of the peak reflected power over inland bodies of water due to the scene heterogeneities should be accounted for in designing retrieval algorithms to map wetland extent.

1. Introduction

Wetlands are areas that are permanently or intermittently inundated or saturated, and support a wide range of vegetation types and ecosystems. Water stored in wetlands is an important component of terrestrial water storage as it affects not only local hydrology and ecosystems, but also surrounding floodplains, and plays a significant role in the emission of global atmospheric methane. Wetlands act as natural flood barriers, temporarily storing excess precipitation/runoff or containing storm surge, and in many areas of the world wetlands are crucial resources for local communities. As the coupled water and carbon cycles accelerate and intensify in a changing climate, our ability to adapt and mitigate will depend on improved measurements of wetland (including flooding resulting from severe weather) extent and changes globally and frequently. Quantitative assessments require characterization of wetland dynamics across time scales from days to years and spatial scales down to sub-km. Nevertheless, a complete and consistent map of global wetlands still needs to be obtained as the Ramsar Convention (Ramsar Convention, 2015) calls for a wetlands inventory and impact assessment. In particular, extensive flooding associated with hurricanes and other severe weather events is becoming more commonplace, affecting the lives of millions of people worldwide. The ability to respond to emergencies rests on the knowledge of the localization and extent of the affected areas, which might be changing over the course of days or less.

Existing remote-sensing methods for global wetland and flood mapping include optical, hyperspectral, and microwave techniques, all presenting strengths and weaknesses associated with their electromagnetic frequency of operation, the mission design and/or the timely availability of the data. For instance, the upcoming Surface Water and Ocean Topography (SWOT) mission carrying a Ka-band radar will be able to map rivers and other terrestrial open water bodies at very high spatial resolution (< 100 m) (Fjørtoft et al., 2014; Grippa et al., 2019), but the repeat frequency of 22 days will not be sufficient for observing

* Corresponding author.
E-mail address: loria.3@osu.edu (E. Loria).

https://doi.org/10.1016/j.rse.2020.111825
Received 1 November 2019; Received in revised form 3 April 2020; Accepted 7 April 2020

the rapid change in surface water dynamics at the tropics (Brivio et al., 2002; Oberstadler et al., 1997). One specific difficulty is due to the intrinsic heterogeneity of wetlands, presenting different types of vegetation, varying over relatively small spatial scales, and partially or totally obstructing the water underneath. At the NASA 2018 Workshop of the Terrestrial Hydrology Program (Pavelsky and Minear, 2018), an international community identified key science questions and measurement requirements for inundation extent data products, recognizing that the current data products are not well validated and do not meet the required resolution. Significantly, errors in determining the extent of wetland inundations and their dynamic changes limit our ability to assess their contributions to the release of methane into the atmosphere, a potent green house gas affecting Earth's climate (Zhang et al., 2017).

GNSS Reflectometry is an emerging remote sensing technique first proposed for ocean topography and winds (Martin-Neira, 1993; Garrison et al., 1998). It relies on the availability of signals transmitted by the GNSS networks that are collected by specially-designed receivers after bouncing off the Earth's surface in a bistatic radar configuration. This concept takes advantage of the ever-increasing number of GNSS transmitting satellites, and can yield many randomly distributed measurements with global distribution. The receiving system is relatively simple and economical to deploy in low Earth orbit, resulting in constellations of receivers that enable much higher temporal sampling frequency as compared to a single satellite (Chew et al., 2017).

The first space-based experiment that shed light on the potentials of reflectometry for a range of applications in addition to ocean wind speeds was the Surrey Satellite Technology Ltd. (SSTL) UK-DMC-1 satellite launched in 2003 (Gleason et al., 2005). This was followed by TechDemoSat-1 (TDS-1), a near-polar orbiter carrying a suite of instruments including a (SSTL SGR-ReSI) GPS receiver, launched in 2015 (Unwin et al., 2020). Shortly after, the NASA Venture Cyclone GNSS (CYGNSS) mission was launched in December 2016, consisting of a constellation of eight small satellites each flying a (SGR-ReSI-derived) GPS receiver as part of their payloads to measure wind speeds in hurricane conditions (Ruf et al., 2016). Each receiver collects scattering contributions in the (primarily) forward scattering direction from an area around the specular reflection point, determined by delay and Doppler filters designed to obtain a surface selectivity by coherent integration in the receiver (Zavorotny and Voronovich, 2000). By cross correlating the transmitted signal along the propagation path with a replica, a sequence of 1-ms coherently integrated reflection waveforms is generated, which are subsequently summed incoherently over 1-second intervals yielding a series of independent reflection measurements. These measurements are given as Delay Doppler Maps (DDM).

Immediately following the availability of data from TDS-1, a number of studies in the community of GNSS-Reflectometry started focusing on reflections over wetlands (Zuffada et al., 2016; Chew et al., 2016; Nghiem et al., 2017) and further intensified since analysis of the CYGNSS data began showing the ability to identify small-scale land features such as rivers and bodies of water even partially obstructed by vegetation. In (Nghiem et al., 2017; Zuffada et al., 2017), based on DDM characteristics such as peaked (limited spread in delay and doppler) and symmetric shape, and very high reflected peak power, it was hypothesized that over wetlands there are strong coherent specular reflections in the collection area of the signal (defined by isorange and isodoppler zones), originating from (even small) areas of standing water, resulting in the measurements' magnified sensitivity to water because of its high electric permittivity and relatively smooth surface compared to dry land and/or vegetation. Plots of peak power, corresponding to CYGNSS measurements' specular points falling in a given cell, aggregated over a period of time, and displayed over large regions with complex hydrology such as the Amazon basin clearly showed the potential of CYGNSS to “map” surface hydrology of intricate scenes at the continental level (Fig. 1).

When forming these maps, it is typically assumed that the peak of the reflected power is dominated by coherent scattering and hence can be represented by a simple radar equation based on the Friis formula that expresses its dependence on the reflection geometry and range, antenna gain, transmitted power and surface reflectivity (Chew et al., 2017). Additionally, it was assumed that the contribution to the peak power comes only from the first Fresnel zone (FFZ), thus implying that the measurement resolution, driven by the size of the FFZ, is much higher than in the case when incoherent scattering is dominant (in which case it is determined by the GPS pseudorandom noise (PRN) code chipping rate). This simple relationship has introduced the surface reflectivity as a working parameter that can be retrieved from the DDM and whose range of variability was first associated with the percentage of water in the measurement footprint (Chew et al., 2016). However, it was found that determining how much water is in the footprint is difficult especially in cases of small percentage values, where the corresponding variability of the surface reflectivity can be quite high. It is easier to associate the changes of surface reflectivity to the state of the scene in a binary fashion, such as determining the presence or absence of standing water (in any amount) over a period of time (Chew et al., 2018; Morris et al., 2019). In particular, both of these studies show that surface reflectivity changes can be correlated to before and after flooding events by establishing a threshold of surface reflectivity that discriminates between the two conditions.

In making the above simplified assumptions one neglects the effects of roughness, a confounding variable since it might look like contributions from vegetation or variations in topography/reflection geometry/transmitted power/antenna pattern. Furthermore, since the receiver performs the cross correlation at the same 1-msec rate on land as it does on water, the collection area for a given DDM bin as defined by the isorange/isodoppler lines is far larger than the first Fresnel zone (or a small number of Fresnel zones). This implies that it is arbitrary to talk about spatial resolution in terms of Fresnel zones, but rather we should focus on whether the DDM peak power is determined by one or more Fresnel zones only. This point is not unimportant when talking about frequency of measurements, and coverage. In practice, a measurement is assigned to the point along the reflection track that corresponds to the specular reflection, as provided by the CYGNSS project. However, the footprint is strictly speaking still potentially affected by the isorange/isodoppler curves across track and its along track integration.

In this paper we take a critical look at the basic assumptions of earlier work, and we investigate how scattering is affected by the size and topology of surface water bodies such as rivers and lakes, and whether realistic scenes are expected to produce a range of peak reflected power by virtue of their complexity, depending on how they are sampled. In such cases, knowledge of this natural variability can help to better interpret the observed signal and its derived geophysical parameters. The ultimate goal is understanding the potential of CYGNSS to map hydrological features at much smaller scales than those reported in earlier work. Section 2 discusses scattering from rough surfaces and present heterogeneities described by complex boundaries between highly reflecting (including attenuation due to vegetation) and completely absorbing media, for the purpose of identifying the coherent and incoherent components of the scattering. Next, Section 3 discusses the sources of variability in the peak received power as well as the spatial resolution of the coherent scattered signal, specifically how it is affected by the scene complexity and boundaries. Section 4 then presents simulated CYGNSS measurements over a highly complex yet simplified hydrology basin, providing an interpretation of actual measurements at this large scale. Section 5 presents a comparison between the modeled and the measured CYGNSS reflections over a lake, as a first validation of our scattering model.

2. Coherent scattering model for inland water bodies with complex geometries

This section describes the coherent scattering model for CYGNSS

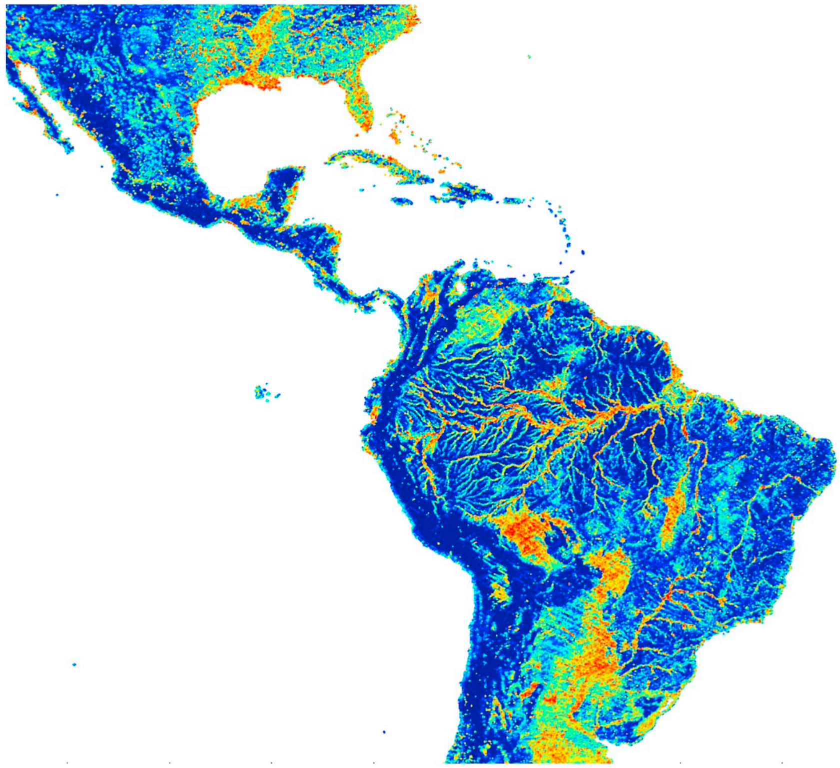

Fig. 1. CYGNSS measured SNR aggregated over 60 days at their reported specular locations over the Americas, showing sensitivity to inland waters. Colour scale goes from blue (0 dB) to red (25 dB). (For interpretation of the references to colour in this figure legend, the reader is referred to the web version of this article.)

measurements that was developed in this work and its specific application to inland water bodies with complex geometries.

2.1. Theoretical considerations for coherent scattering

First airborne experiments that studied the use of GNSS bistatic reflections for remote sensing purposes considered an ocean surface as the object of interest. If the ocean surface is ideally calm these reflections are coherent, which means that the phase of the incoming EM wave is preserved, and the reflected wave would travel in a nominal specular direction. However, because of wind action on the ocean its surface becomes rough, which leads to diffuse, incoherent scattering of EM waves. The angular spread of these diffusely scattered waves around the nominal specular direction depends on surface roughness Δh which can be characterized by the Rayleigh parameter (Beckmann and Spizzichino, 1963),

$$R_a = 2\pi \langle \Delta h^2 \rangle^{1/2} cos(\theta)/\lambda. \tag{1}$$

For winds above 3–4 m/s and long enough fetch, the surface roughness Δh is such that this parameter for L-band signals and small enough incidence angle θ is much greater than one, indicating a total extinction of the coherent component and an onset of the strong diffuse scattering regime. For $R_a < 1$, theoretical models predict a regime of weak diffuse scattering accompanied by a partially coherent component (Voronovich and Zavorotny, 2017). However, because of a high prevalence of swell in the world's oceans, it is rare to have values of $R_a < 1$, and thus there is a lack of coherent GNSS reflections, even at weak winds below 3 m/s. Reflections of GNSS signals from relatively small inland bodies of waters such as lakes, reservoirs, wetlands and rivers exhibit both the coherent and weakly-diffuse incoherent component in the DDM. This is due to overall weaker winds, shorter fetches, and absence of swell for these water basins.

In the general case of both coherent and incoherent scattering, the mean value of the DDM takes the form of a bistatic radar equation:

$$\langle |Y(\tau, f; t)|^2 \rangle = \frac{\lambda^2 P_t G_t}{(4\pi)^3} \iint \frac{G_r \chi(f, \tau)^2}{R_1^2 R_2^2} \gamma \sigma_{pq}^0 dS, \tag{2}$$

where $P_t G_t$ forms the transmitter's Effective Isotropic Radiated Power (EIRP); G_t and G_r are the transmitter and receiver antenna gains, respectively; R_1 is the range from transmitter to the point on the surface; R_2 is the range from the surface to the receiver; χ is the Woodward Ambiguity Function (WAF); γ is the attenuation factor due to vegetation canopy (if present); ${\sigma_{pq}}^0$ is the total polarization-dependent normalized bistatic radar cross section (NBRCS), with p and q the incident and scattered polarizations, respectively.

We will then represent the total received power as a sum of its coherent and incoherent components (Voronovich and Zavorotny, 2018):

$$\langle |Y(\tau, f; t)|^2 \rangle = \langle |Y_{coh}(\tau, f; t)|^2 \rangle + \langle |Y_{inc}(\tau, f; t)|^2 \rangle. \tag{3}$$

Many previous works have examined the coherent component of the microwave power bistatically scattered by a rough surface (Voronovich and Zavorotny, 2018; Fung and Eom, 1983; Ulaby et al., 2014). Based on those models, for a large plane surface covered by a small-scale roughness, the coherent component of the power is given by:

$$\langle |Y_{coh}(\tau, f; t)|^2 \rangle = \frac{P_t G_t}{4\pi (R_t + R_r)^2} \frac{\lambda^2 G_r}{4\pi} |\chi(\tau, f)|^2 \gamma |\Gamma|^2 \psi, \tag{4}$$

where the surface roughness loss term $\psi = e^{(-4{R_a}^2)}$ depends on the Rayleigh parameter R_a and Γ is the Fresnel reflection coefficient. The coherent component exists only in a small angular region around the nominal specular direction (Ulaby et al., 2014).

Several parameters in (4), such as G_r, P_t, or Γ may vary in time and/or across the surface. However, for the time and spatial scales we are evaluating, it is possible to assume that these parameters in a given scene are constant. This equation is an analog of the image theory version of the Friis formula and is well known in radar applications (Ulaby et al., 1986).

Here, we can introduce the surface reflectivity, which is often used in these GNSS-R applications. The Surface Reflectivity (*SR*) is found by rearranging the image theory Eq. (4) for an effective value of the reflection coefficient, Γ, and replacing the received peak power Y^2 with the measured signal-to-noise ratio (SNR). Because the SNR is not exactly related to the received, incident power level the equation for the *SR* is proportional to the measured SNR from the DDMs (Chew et al., 2018). This relation can be written as:

$$SR \propto \frac{SNR(4\pi)^2(R_t + R_r)^2}{P_t G_t G_r \lambda^2}. \tag{5}$$

It is important to note that CYGNSS measurements of SNR are subject to varying noise power and instrument gain, among other effects that can make this proportionality not exactly linear.

Eq. (4) reveals that the measured DDM is proportional to the product of three parameters related to properties of the scattering object. Those are: the attenuation factor due to vegetation canopy γ, the power Fresnel reflection coefficient $|\Gamma|^2$ of the mean surface, and the decorrelation factor ψ, which is driven by the surface roughness. In order to retrieve one of them we need to know the other two. For CYGNSS reflections at most incidence angles, the decorrelation factor predicts that coherent power only exists for $\Delta h < 5$ cm. If the object is perfectly flat, $\psi = 1$, and if there is no vegetation, $\gamma = 1$, then the DDM measurements can be used for calibration purposes, i.e. for estimating instrumental factors entering (4). The uncertainties associated with these factors are very important and might play a critical role in the assessment of the feasibility of CYGNSS and other GNSS-R mission retrieval algorithms (see e.g., (Wang et al., 2019)).

The adoption of Friis formula in (4) to describe the DDM coherent component in the case of land and wetlands scenes is not adequate if those scenes are heterogeneous. In the case of relatively small water bodies, or for heterogeneous scenes, Y_{coh} cannot be expressed by such a simple expression as in (4). For arbitrary shaped scattering scenes, which are being considered in our study, we seek a numerical solution for scattered fields with complex amplitudes as described by diffraction integrals.

2.2. Coherent scattering model for inland bodies of water

In what follows, we present our model for coherent scattering from inland bodies of water with arbitrary shapes. To begin, the scattered electric field is approximated using the Kirchhoff diffraction integral (Bass and Fuks, 1979):

$$E_s(f) = E_0\frac{jk}{4\pi}\iint \frac{p}{R_1R_2}exp[-jk(R_1 + R_2)]dS, \tag{6}$$

where E_s is the scattered field at the receiver, p describes amplitudes, phases and polarizations of the electric fields on the surface S and the impedance of the scattering medium; R_1 is the range from transmitter to the point on the surface; R_2 is the range from the surface to the receiver. E_0 describes the amplitude of the transmitted field. It is well-understood that the Kirchhoff approximation has its limitations in accuracy (Thorsos, 1988). Since we are looking at reflections in the specular direction, this approximation is sufficient to describe the reflecting surface.

We assume a smooth surface and follow the results in (Beckmann and Spizzichino, 1963). The effects of polarization are only considered when calculating a reflection coefficient Γ for the right hand circularly-polarized to the left hand circularly-polarized case,

$$p = \sqrt{\gamma\psi}\,\cos(\theta)\Gamma(\theta), \tag{7}$$

where θ is the incidence angle at the specular point on the surface. Over the surface area we are considering θ does not vary significantly and we can treat it as constant. The components of (7) may vary over the surface to capture different heterogeneous scenes. It is assumed that these variations over the surface occur at a spatial scales much larger than a wavelength, making the approximation sufficiently accurate.

The form of (6) is only applicable to a static scenario. Since the geometry of our receiver and transmitter is dynamic and measurements of the field are integrated over a coherent integration period, it is important to carefully consider how time variation is incorporated into our model. We will explicitly denote the scattered field at the receiver at time t as

$$E_s(f;t) = E_0\frac{jk}{4\pi}\iint \frac{p(t)}{R_1(t)R_2(t)}exp[-jk(R_1(t) + R_2(t))]dS, \tag{8}$$

where, since the change in time is slow relative to the speed of light, we utilize the quasi-static approximation as in (Zavorotny and Voronovich, 2000). This approximation does not address relativistic effects (which are negligible) but does accurately capture Doppler shifts over the surface. It requires that over the time period the signal is processed, all terms in (8) besides the phase be constant.

Next, we will focus on a specific time interval $[t_1, t_2]$ with mid-point t_m. The duration of this interval (which we later use as our coherent integration interval) is short relative to the dynamics of the receiver and transmitter. Consequently, we will approximate (8) over this interval by assuming that the effect of the change in amplitude of the integrand is negligible and that the effect of the change in phase is approximately linear

$$E_s(f;t) = E_0\frac{jk}{4\pi}\iint \frac{p(t_m)}{R_1(t_m)R_2(t_m)}exp[-j\phi(f;t)]dS, \quad t \in [t_1, t_2] \tag{9}$$

where ϕ is the phase over the surface,

$$\phi(f;t) = k(R_1(t_m) + R_2(t_m)) + 2\pi f_D(t_m)(t - t_m), \tag{10}$$

and the linear variation in phase f_D is the Doppler shift at a particular location on the surface,

$$f_D(t') = \frac{1}{c}\frac{\partial}{\partial t}(R_1(t) + R_2(t))|_{t=t'}. \tag{11}$$

Note that, if the duration of the coherent integration interval were to increase appreciably, it could be necessary to extend this to a piecewise linear approximation over the interval.

Next, we recognize that (10) applies for a single frequency but our GNSS signal technically occupies a narrow, but non-negligible bandwidth. Over the small frequency range of the GNSS signal $f \in [f_1, f_2]$, we will assume that the magnitude of the field is constant and the phase varies linearly with frequency. The field is then,

$$E_s(f;t) = E_0\frac{jk_c}{4\pi}\iint \frac{p(t_m)}{R_1(t_m)R_2(t_m)}exp[-j\phi(f_c;t) + j2\pi f\tau_d]dS \tag{12}$$

where f_c is the center frequency, k_c is the wavenumber at the center frequency, and phase now incorporates a linear phase variation with frequency τ_d (i.e. the group delay) which varies over the surface.

Now, let us assume the transmitter transmits signal *r(t)* that is modulated onto the incident field. The signal at the receiver *x(t)* is given by the convolution

$$x(t) = \int E_s(f;t)R(f)e^{j2\pi ft}df \tag{13}$$

which is the standard form for a linear time-varying (LTV) system where *R(f)* is the frequency domain representation of *r(t)*. Substituting (12) into (13), we get

$$x(t) = E_0\frac{jk_c}{4\pi}\iint \frac{p(t_m)}{R_1(t_m)R_2(t_m)}e^{-j\phi(f_c;t)}\left[\int R(f)e^{j2\pi f(t+\tau_d)}df\right]dS \tag{14}$$

$$= E_0\frac{jk_c}{4\pi}\iint \frac{p(t_m)r(t + \tau_d)}{R_1(t_m)R_2(t_m)}e^{-j\phi(f_c;t)}dS \tag{15}$$

The receiver forms the cross-correlation Y between a locally generated reference signal *r(t)* and the received signal *x(t)*. The cross-correlation occurs over the time interval $t \in [t_1, t_2]$ at delay offset τ and frequency offset δf,

$$Y(\tau, \delta f) = \frac{1}{T_c} \int_{t_1}^{t_2} x(t) r^*(t-\tau) e^{j2\pi\delta f t} dt \quad (16)$$

where $T_c = t_2 - t_1$ is the coherent integration time. Substituting (15), we arrive at the form

$$Y(\tau, \delta f) = \frac{jk_c}{4\pi} \iint \frac{p(t_m)\chi(\tau - \tau_d, \delta f - f_D)}{R_1(t_m) R_2(t_m)} exp[-jk_c(R_1(t_m) + R_2(t_m))] dS \quad (17)$$

where we have made an approximation that the coherent integration time T_c is sufficiently long for the cross-correlation value to converge to its expected value

$$\frac{1}{T_c} \int_{t_1}^{t_2} r(t + \tau_d) r^*(t - \tau) e^{j2\pi\delta f t} e^{j2\pi f_D t} dt \sim \chi(\tau + \tau_d, \delta f - f_D) \quad (18)$$

For our study, we will focus on a small area around the specular point, and it is sufficient to approximate the transmitter and receiver antenna patterns as constant, and the power of the reflected signal after coherent integration is

$$|Y(\tau, \delta f)|^2 = \frac{G_r G_t P_t}{(4\pi)^3} \left| \iint_S \frac{jk_c \sqrt{\gamma\psi} \cos(\theta) \Gamma(\theta) \chi(\tau + \tau_d, \delta f - f_D)}{R_1 R_2} exp[-jk_c(R_1 + R_2)] dS \right|^2, \quad (19)$$

where the geometric quantities are evaluated at t_m. Changes in the CYGNSS received antenna pattern projected onto the scattering surface area were deemed to be negligible (< 0.1 dB) over the $\sim$10 km surface area contributing to the coherent power. The form of (19) is an extension of (4) to coherent scatterers with complex boundaries.

The above model only applies to the coherent component of the reflection. Real scenes will also contain non-coherent scattering from rough surfaces over either water or land. In this case, the total DDM would be formed by the sum of the coherent and non-coherent components of the scattered fields. The form of the non-coherent component as well as the basis behind the summation of coherent and diffuse components has been extensively reported elsewhere (Zavorotny and Voronovich, 2000; Voronovich and Zavorotny, 2018).

2.3. Numerical implementation

In order to solve the integral numerically, we must discretize the surface. When implementing the discrete scattering integral, the surface must be evaluated over a large enough area to accurately account for all of the contributions to the received electric field. The span of the grid (on which surface S is located) was 10 km × 10 km. A large set of grid sizes were examined to verify that solutions for the received power converged. In addition to the surface extent, the phase must not change too quickly over each patch area dS in the integral. That is, we want the received phase from the center of the patch to be representative of the edges as well. In addition to the total extent of the surface we must evaluate the integral over, the discretization size is also of importance. If the size of each differential area dS in the numerical implementation of the integral is too large, the surface will be under-sampled. In (19), most of the terms vary slowly over the total grid surface. The two main terms that change rapidly in the integral now are the phase term and the boundaries of the integration that describe the scattering surface, S. The amplitude of excitation over the grid also varies slowly, leading to the main contributor to changes in the received power being the interaction between the Fresnel zones, or phase on the surface, and the shape of the scatterers themselves. In order to get an accurate solution from the integral equation, the size of each patch on the surface must be small enough to sample the most rapidly varying quantity, which is generally the phase. We have found that values below $\sim 30\lambda$ produce minimal phase variation at the edges of the grid, and lead to a converged solution for the received power.

In this paper, we approximate the surface as either scattering with a Fresnel reflection coefficient Γ, or non-scattering with a reflection coefficient of zero. In reality, a small amount of diffuse scattering also occurs from the portion of the surface that is not electrically smooth enough to contribute to the coherent signal power. However, this contribution is generally small in comparison to the coherent power in the peak of the DDM. The goal is to utilize a simulator in order to evaluate the effective scattering area of coherent reflections, as well as test the efficacy of current wetland inundation retrieval algorithms.

This scattering integral was implemented inside the CYGNSS End-to-End Simulator (E2ES) (O'Brien, 2014). The E2ES is a detailed software simulator written to emulate the GNSS-R bistatic signal scenario, and models all the steps of forming the DDMs on CYGNSS. For this paper, we have extended this E2ES to include coherent scattering from heterogeneous surfaces, as described above. The simulator allows us to evaluate scattering scenes with realistic sets of parameters in order to examine the nature of the variability in the scattering scenes.

3. Sources of variability in the peak power of coherent scattering

Having defined our coherent scattering model, several important sources of variability in the peak power that will affect retrieval algorithms can be identified. First, the size and shape of the coherent scattering surface will introduce variations in the amplitude. In this section, we begin by discussing how the spatial resolution is more complex that previous work has assumed. We also discuss how surface roughness and vegetation impact the scattered power.

3.1. Spatial resolution of coherent scattering

It is important to better understand the spatial resolution of CYGNSS measurements when coherent scattering is present. While it is commonly approximated that only the spatial area corresponding to the first Fresnel zone contributes to coherent scattering, we utilize our model to illustrate that the actual question of spatial resolution in heterogeneous scenes is more complex. Note that our analysis focuses on the spatial resolution after coherent integration only.

To begin, the phase ϕ of field over the surface is captured in the exponential term of (19),

$$\phi(r) = k_c(R_1((r)) + R_2(r)), \quad (20)$$

where r is the position vector that varies over the surface. Fig. 2 shows a plot of this function over the surface of the Earth for a typical CYGNSS scenario. In this case, the altitude of the transmitter is 20,160 km (typical GPS satellite altitude), the altitude of the receiver is 500 km, and the incidence angle is 50 degrees. The center of the surface corresponds to the specular point and the phase has been made relative to this point. The phase forms Fresnel zones – concentric regions around the specular point that corresponds to a shift of 180 degrees of phase. Note that although the wavelength at the GPS L1 frequency is only 19 cm, the distance over which the phase changes on the surface according to (20) is much larger.

Several important properties are illustrated in Fig. 2. First, the first Fresnel zone is special in that it represents an elliptical region (rather than a ring) over which the phase varies slowly by one period. The major axis of the first Fresnel zone is approximately 1 km and will change based on the incidence angle. Second, for the case of CYGNSS where the receiver and transmitter are very far from the surface, the zones are symmetric and centered around the specular point. Third, the surface area of each zone is nearly identical, which can be confirmed via numerical integration. This point can be seen more clearly in the right-hand plot of Fig. 2, where each of the first 7 zones are delineated and colour-coded. Finally, it should also be noted that the size of the Fresnel zones are much smaller than the size of the WAF (defined by the intersection of isorange and isodoppler lines) projected onto the surface. This is approximately 20 km in major axis for the CYGNSS case where $T_{coh} = 1ms$, and describes the typical CYGNSS resolution for non-coherent scattering.

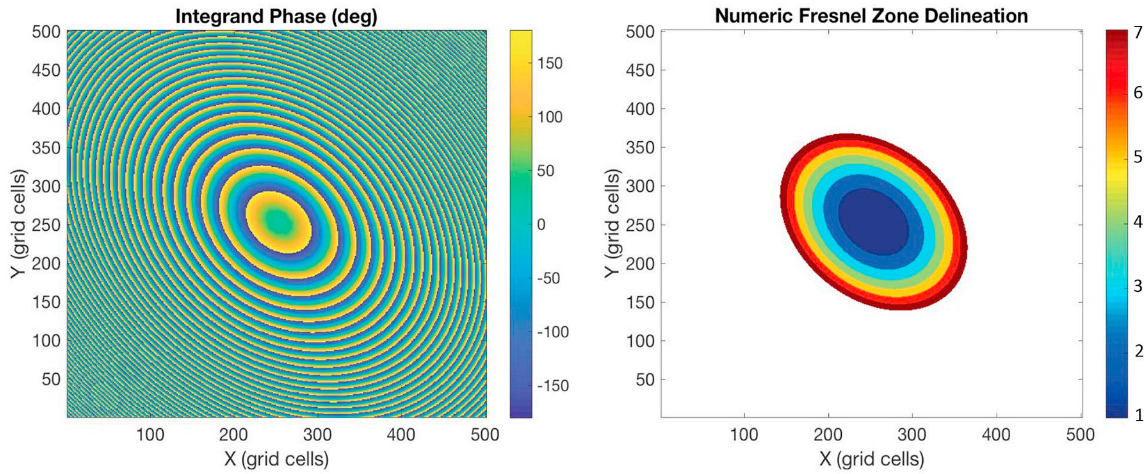

Fig. 2. Example of the reflected signal phase (degrees) over a 3.5 km simulation grid, which shows the Fresnel zones. This case uses a typical CYGNSS-GPS geometry and a 50 deg. incidence angle.

In order to illustrate the contributions of different Fresnel zones, the scattering integral in (19) was evaluated to predict the peak SNR received from a simple circular-shaped scatterer as its radius increases. The nominal CYGNSS-GPS geometry with 50 deg. incidence angle was chosen for this case. The results, shown in Fig. 3, indicate that as the scatterer size increases between zero and the radius of the first Fresnel zone, there is a rapid increase in reflected power as a function of area-squared. The power stops increasing as the radius begins to incorporate the surface area where the phase relative to specular point exceeds 90 degrees. As the size increases further, the received power converges to the power level predicted by image theory (dashed red curve). However, there is ripple (> 3 dB) as contributions from higher Fresnel zones add constructively or destructively. Note that the total power can exceed the level predicted by image theory. We also observe that the power can drop below the predicted level even when the first Fresnel zone is full. Contributions by the various Fresnel zones are either constructively or destructively changing the total electric field at the receiver. The exact way in which complex shapes will affect the total received power is not known a priori. The amplitude of these oscillations in the received power are significant because they are large enough to confound the effects on the peak power due to other wetlands parameters (such as vegetation attenuation) that we are interested in retrieving, and adds an ambiguity to the surface scatter size. For some simple scatterer shapes, closed-form solutions can be found (Balakhder et al., 2019). The interactions between the scattering surface and the Fresnel zone geometry can affect the received phase of the signal as well.

Fig. 4 shows the case where the incidence angle is set to 0 degrees. Here, the Fresnel zones are now circularly shaped. Because the circular scatter now matches the shape of the Fresnel zones, we observe that the magnitude of the reflected signal can vary as the scatterer size increases. Since the area of each Fresnel zone is nearly identical and the other parameters (antenna gain, range, etc) cause negligible variations in the amplitude between subsequent zones, the integral over each zone cancels with the previous one nearly perfectly. Although the scatterer shape is a degenerate example, it illustrates the point that the contributions from Fresnel zones other than the first are clearly not negligible. In fact, we would find that this oscillatory behavior extends for hundreds of Fresnel zones until it is finally dampened by the WAF and converges. Although this result was for zero degree incidence, this result would occur for any incidence where the scatterer were made to be the same shape as the Fresnel zones.

Through this illustration, it is clear that it is an over simplification to state that coherent scattering observed by CYGNSS is measuring only the contents of the first Fresnel zone or even the first several Fresnel zones. Instead, a more accurate description is as follows. When the

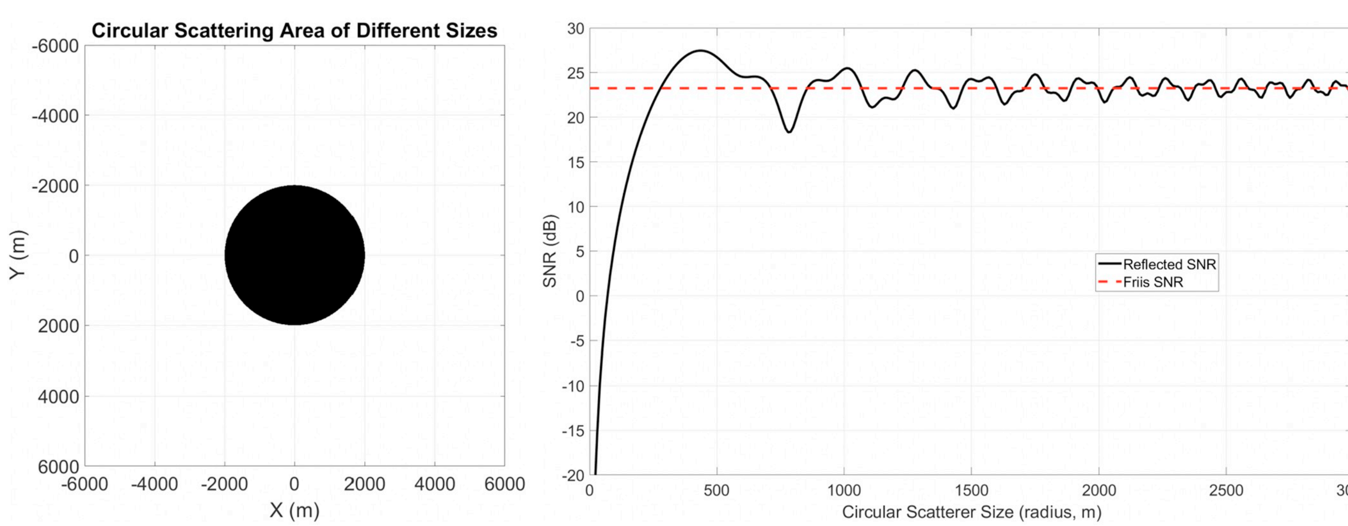

Fig. 3. SNR vs. radius of circular scatterer $\theta = 50$. Dashed red line shows image theory result. (For interpretation of the references to colour in this figure legend, the reader is referred to the web version of this article.)

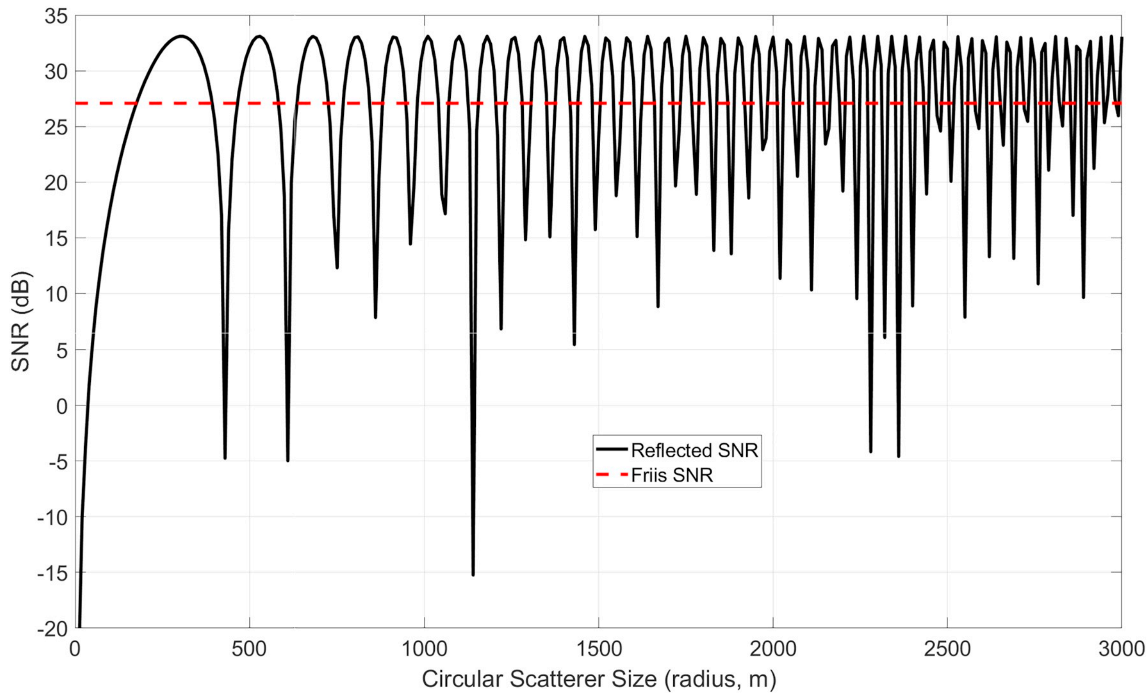

Fig. 4. SNR vs. radius circular scatterer with $\theta = 0$. Dashed red line shows image theory result. (For interpretation of the references to colour in this figure legend, the reader is referred to the web version of this article.)

scatterer is small and is located in only a portion of the first Fresnel zone, its scattered power is directly proportional to its area squared. If its size occupies the entirety of the first Fresnel zone, then the magnitude of the reflection has a variation (often > 3 dB) that depends very sensitively to the shape of the boundary, even if this boundary extends several hundred Fresnel zones away.

Fig. 5 shows the reflected power from a circular shaped scatterer 1 km in diameter which is moved away from the specular point. In this case, we observe that there is significant reflected power even as the location of the scatterer moves well outside the first Fresnel zone. Although the magnitude has decreased substantially, there is still sufficient SNR to receive the signal. This effect was shown both theoretically (Balakhder et al., 2019) and experimentally (Geremia-Nievinski et al., 2016).

Based on these examples, it is clear that the resolution of coherent scattering cannot simply considered to be the first Fresnel zone. Contributions from the scatterer's boundary or scatterers located outside the first Fresnel zone will introduce variability in the magnitude of received signal at a given measurement point, identified by the specular reflection point. It should be noted that the results presented here included motion of the receiver only during the coherent integration interval. If additional non-coherent summation of measurements is performed (as is done to produce the CYGNSS DDMs), then the along-track motion would also need to be addressed in understanding of the total spatial region impacting the measurement. Further confounding variables that affect the peak coherent power in wetland scenes include attenuation from both vegetation and small-scale surface roughness. The nature of these two effects are introduced and further discussed in the following paragraphs.

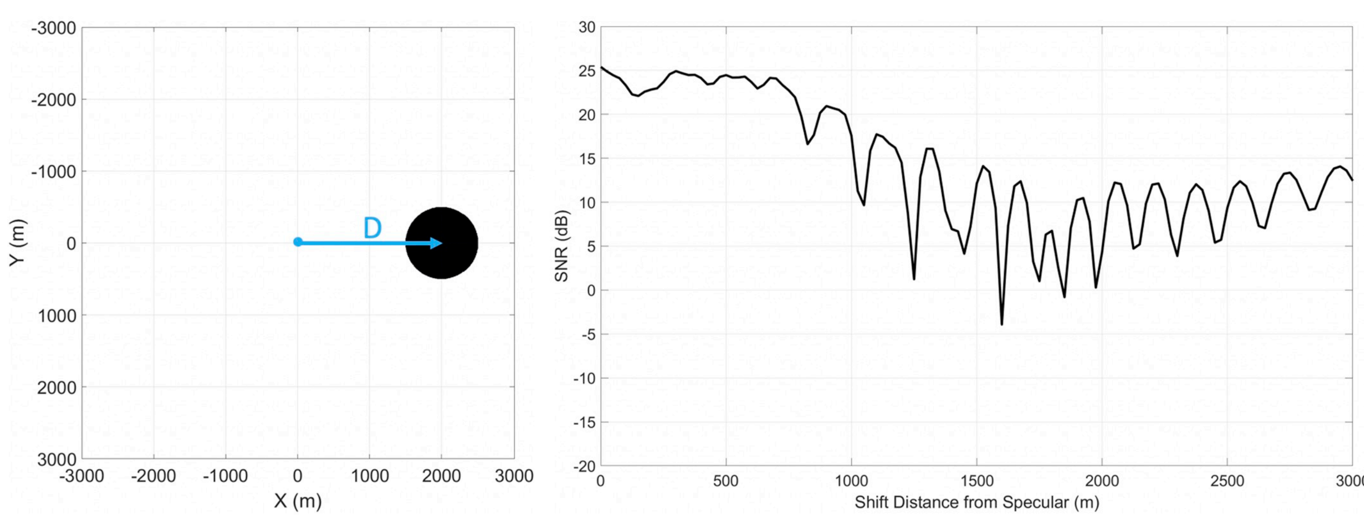

Fig. 5. SNR vs. offset of a 1 km diameter circular scatterer.

3.2. Vegetation attenuation effects

Most scattering theoretical models treat the vegetation canopy as a uniform layer consisting of random scatterers (Fung and Ulaby, 1978). The vegetation layer is described either as a continuous medium or as a discrete medium, although the latter is used most frequently. In the discrete case, the vegetation canopy is subdivided into single elements, where each one is modeled electromagnetically (i.e. permittivity, scattering cross section, and extinction cross section, etc.), providing more rigorous models (Karam et al., 1992; Ulaby et al., 1990). For most crops and low vegetation, the vegetation nadir optical depth τ_0 can be written as a function of the plant water content (PWC), in $[kg/m^2]$. The following linear relationship is commonly provided in the literature, (Jackson and Schmugge, 1991):

$$\tau_0 = b \cdot PWC. \tag{21}$$

The parameter b is a function of the canopy type/structure, polarization, and wavelength. Previous studies showed that at 1.4 GHz, a value of b within the range 0.12 ± 0.03 was found to be representative for most agricultural crops and low vegetation (Jackson and Schmugge, 1991). The empirical models treat the effect of vegetation on GNSS reflected signals via an additional attenuation factor on the received signal power, (Ulaby et al., 1986; Kerr et al., 2012). This attenuation factor, γ, can be expressed in terms of τ_0:

$$\gamma = exp(-2\tau_0/cos(\theta)). \tag{22}$$

The 2 factor accounts for the two-way attenuation of the GNSS signals along the incident and reflected paths through the vegetation layer. Fig. 6 shows the expected range of attenuation for a set of typical incidence angles and over realistic PWC values (Chan et al., 2013; Saatchi et al., 2007). It can be seen that the expected vegetation attenuation for GNSS reflections can cover a large portion of the dynamic range of CYGNSS SNR values (apprx. 0-24 dB), and can drastically reduce the signal power.

3.3. Surface roughness effects

Small-scale surface roughness plays an important role in determining the total signal power that is specularly reflected. The decorrelation loss variable ψ introduces significant attenuation with even a small amount of RMS height change on the surface. This effect and the transition between coherent and diffuse scattering for inland waters is more thoroughly examined in a companion paper (Zavorotny et al., 2020). As (1) shows, the Rayleigh parameter and thus decorrelation loss is dependent on both the amplitude of the water surface waves and the incidence angle. A few centimeters of RMS height change can strongly reduce the coherent power, leading to additional complications in surface water retrievals. Fig. 7 shows the expected range of attenuation for a set of typical incidence angles and a range of surface roughness (Δh) values. The total extinction of the coherent component occurs rapidly with an increase in RMS height.

3.4. Changes in peak power with incidence angle for the roughness, vegetation, and fresnel zone effects

The roughness parameter ψ can be thought of as an effective surface roughness, as it is sensitive to the electromagnetic wavelength, RMS surface height changes, and the incidence angle. Higher incidence angles leads to smaller changes between the phase of the scattered fields from different parts of the surface, which in turn reduces ψ. However, for vegetation, the higher the incidence angle is, the longer the path is of the signal traveling through the vegetation. This leads to an increase in the attenuation factor, γ. It can be noted that the changes in signal attenuation for ψ and γ have opposite relations to the incidence angle of a given reflection: higher incidence angles for a particular scene with roughness and vegetation will lead to lower ψ, but higher γ. Conversely, then, lower incidence angles results in larger ψ and lower γ. The scale of both of these effects on the peak power are on a similar order as the Fresnel zone effects shown in these simple examples (e.g. Figs. 3, 4, and 5). We still expect the peak power transition between a scene with surface water and a scene without to be large, but the power will be

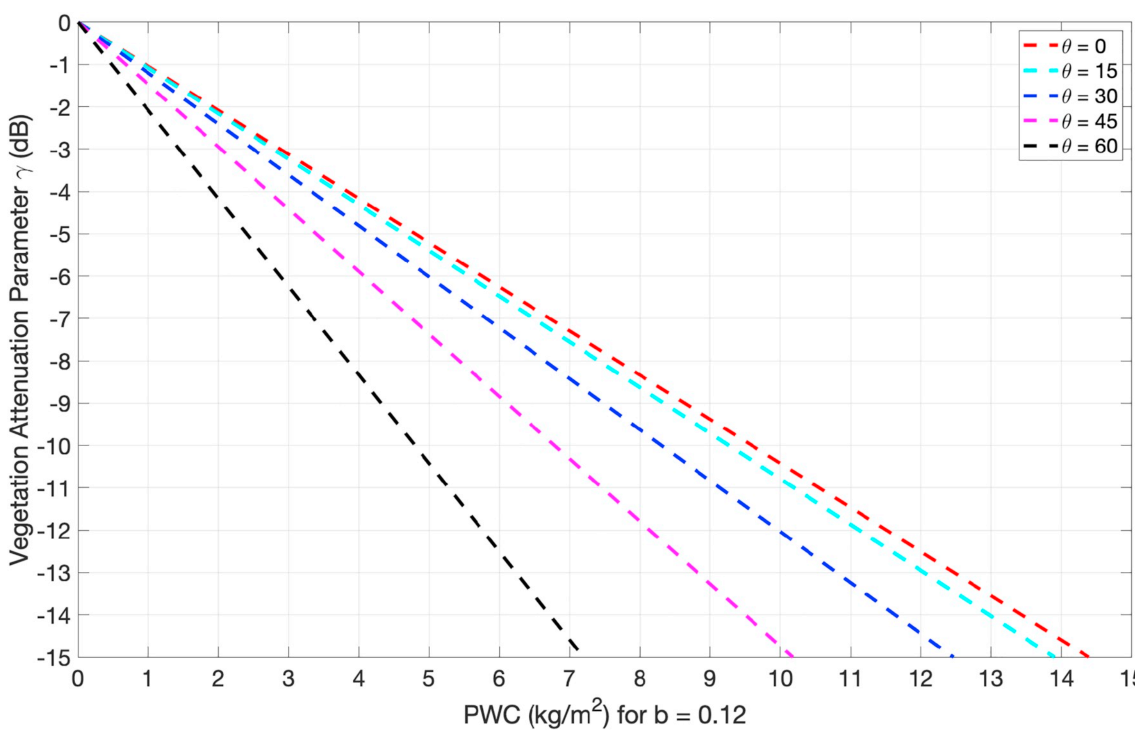

Fig. 6. Vegetation attenuation γ (dB) for increasing PWC with $b = 0.12$ at several incidence angles.

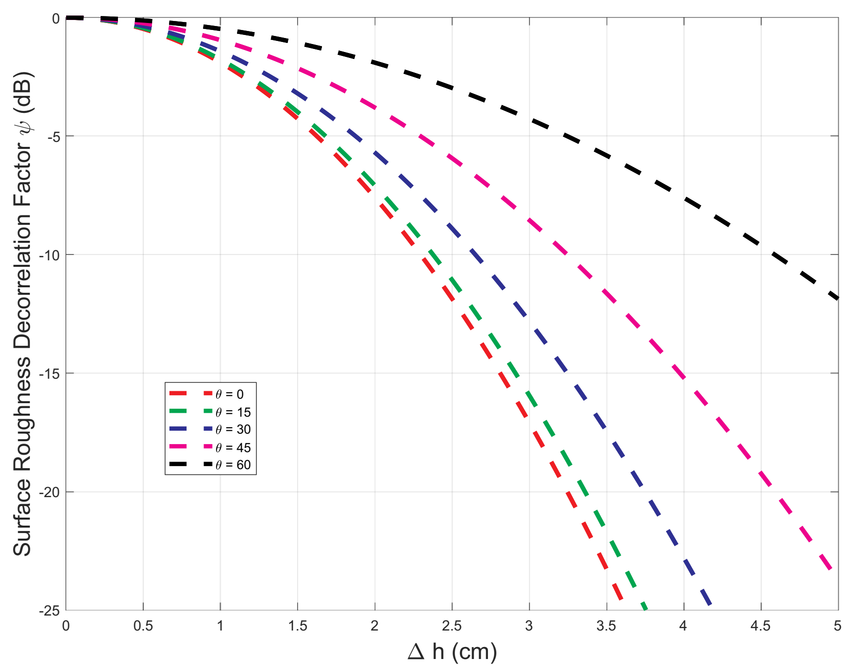

Fig. 7. Surface roughness attenuation ψ (dB) for increasing roughness at several incidence angles.

modulated by both the Fresnel zone behavior as well as the effects of roughness and vegetation, and it may be difficult to disentangle the three. In the next Section, we take a closer look at the scale of the variability in the peak power due to the Fresnel zones and its variation with incidence angle.

4. Simulation study of coherent scattering from complex bodies of water

In wetlands, such as the Amazon River basin, heterogeneous scenes are the ones most often encountered. Fig. 8 shows the MODIS water mask (black is land, white is water) from a typical area along the Amazon River (Carroll et al., n.d.). In this paper we treat the topography of these inland waters as locally flat and include Earth curvature. For these heterogeneous scenes we are interested in, we treat the surface as a binary medium where water is reflecting with a reflection coefficient Γ and land is totally absorbing.

The coherent scattering model was integrated into the CYGNSS End-to-End Simulator. Observations were simulated by taking information for transmitter and receiver geometry, GPS EIRP, and receiver antenna gain directly from the CYGNSS v2.1 data files. This gives us realistic sampling and power levels for the simulation. In order to accurately

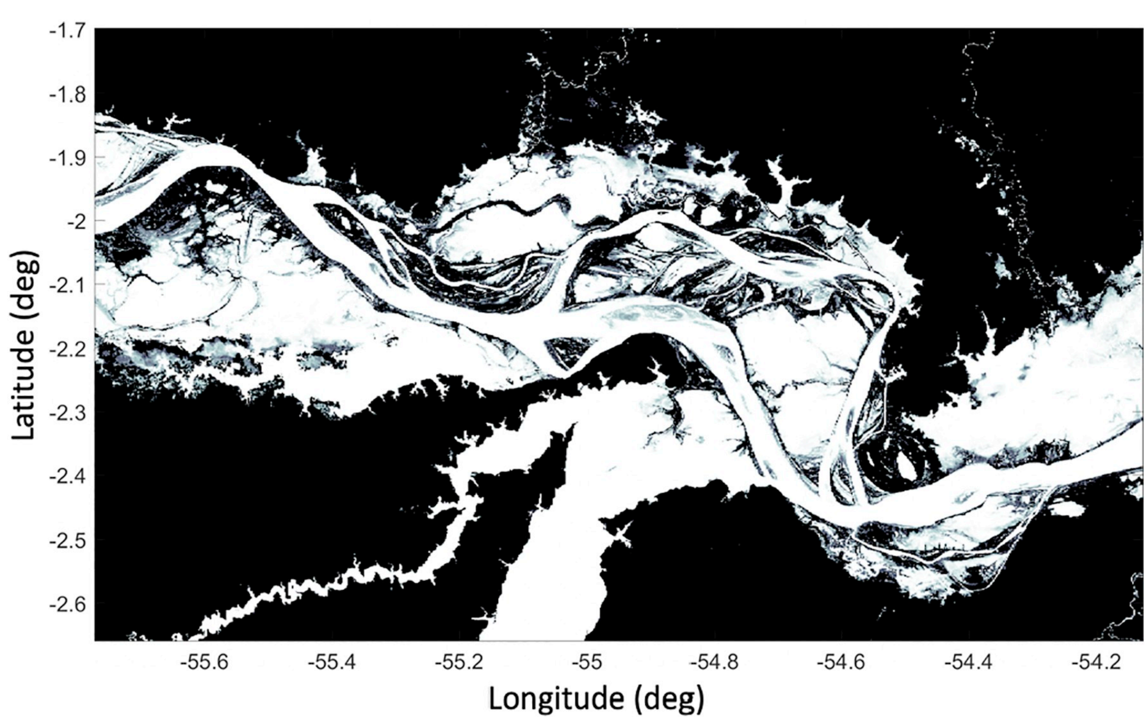

Fig. 8. Example water mask along a small segment of the Amazon River, showing the complex geometry of land and inland waters.

capture the heterogeneity of wetlands scenes, we use the MODIS MOD44W (250 m) dataset for the inland water scenes (Carroll et al., n.d.). The simulated grids accurately capture the realistic mix of inland water and land in the region of interest, which provides a higher fidelity model than a simulation of randomly generated scenarios. This forward model integration in the E2ES framework provides the basis for the simulation of wetland extent and, consequently the formulation of retrieval algorithms.

The next sections study the variability of the reflected signal power. First, the variability as a function of incidence angle is demonstrated over a variety of inland water scenes. Second, the variability of the measured power over a large hydrological basin is simulated and quantified as a function of the amount of water in the first Fresnel zone. These two examples highlight the errors associated with the assumption that the first Fresnel zone defines the resolution of the measurement. Third, a simple retrieval of percentage of water is performed using the simulated data after it has been averaged into a grid in order to quantify impact of this variability in received power.

4.1. Variability with incidence angle

Considering a fixed inland water scene, we first examine how peak reflected power changes by changing the reflection geometry. This way we explore the variability of coherent scattering on the surface due to the complex interactions between the even and odd numbered Fresnel zones, and the heterogeneous scattering surface. While the specular point is fixed, the incidence (θ) and azimuth (ϕ) angles change. In this exercise, the path lengths, antenna gains, etc. have been fixed. For each (θ, ϕ), the expected received power in the specular direction is calculated. Fig. 9 shows the peak SNR of three different scattering scenes over the varying angle pairs. Variance in the received power can be attributed to complex interactions between the scattering surface and Fresnel zones. Large changes in amplitude can be seen (nearly 15 dB) for the same surface for different reflection geometries. This variability is unique to coherent scattering from heterogeneous surfaces and is not expected from diffuse scattering or homogeneous surfaces. The scene over ϕ varies, but is nearly 180 degree symmetric, since for spaceborne receivers, the Fresnel zones are nearly identical with any 180 degree rotation. It is expected that this large variability in the received peak power, even for the same scene, will lead to errors in the retrieval accuracy of surface water content. Over the next few paragraphs, we discuss how this complex scattering scene affects the current retrieval approaches.

4.2. Variation over large wetlands scenes

For the results presented in this section, 90 days (2017, days 077–167) of CYGNSS ancillary data was used to simulate the sampling of the Amazonian region modeled in Fig. 10. The v2.1 data provided realistic observation values to be used in the simulation for relevant parameters such as the specular point sampling, transmit EIRP, receiver antenna gain, and reflection geometry. Then, for all of these samples, the scattering integral (19) was evaluated using the MODIS data as a truth watermask (Fig. 10). The aggregation of many data points allowed for the examination of statistics relevant to the current retrieval algorithms.

As stated earlier, a common approximation in the GNSS-R community is that the strength of the reflected signal peaks can be approximated as being proportional to the percentage of the first Fresnel zone area that is occupied by inland water. This approximation is predicated on the assumption that the FFZ is the main scattering area, with minimal contributions from other Fresnel zones. We are interested in quantifying the error in this approximation. Using this approach, the fractional water in the FFZ footprint can be estimated by mapping the received power back to an area-squared curve with a manually chosen offset. The received SNR values must first be normalized by a few parameters: receiver antenna gain, EIRP, reflection coefficient, incidence angle, and the transmitter/receiver distances to the specular point. This is equivalent to the *SR* value given in (5) with an additional term for the incidence angle, $\frac{1}{cos(\theta)^2}$. After applying these corrections, the resulting powers can be used to estimate the percentage of water in the FFZ. A plot of the modified SNR (the received SNR values normalized by the previously described parameters) and the corresponding simple area-squared curve is shown in red in Fig. 11. Estimations of the surface water content in the FFZ are formed by mapping the modified SNR value to the red area-squared curve. For a given power value (y-axis), the estimated percentage of water would then be the x-axis value. In the ideal case, all of the simulated data would be situated directly on the red area-squared curve. However, the scatter of peak power around the simple area curve is the result of scattering from outside the FFZ, and provides a source of error in this retrieval method. This scatter has also been observed in CYGNSS data as well (Zuffada et al., 2017).

4.3. Impact on retrieval accuracy

Unfortunately, the peak power scatter under the FFZ-scattering area approximation of Fig. 11 represents a best case scenario with no other confounding variables (such as vegetation or surface roughness) or error sources. There are also additional measurement effects that we must consider in our model. In the CYGNSS data, the measured SNR is actually a peak-to-mean ratio. Therefore, the minimum SNR is based on the noise floor of samples in the DDM. In addition, the GPS L1C/A coded signals that are used by CYGNSS have sidelobes 24 dB below the peak, so the maximum SNR is approximately 24 dB. This is due to the way in which CYGNSS measures SNR, which is really a peak-to-mean ratio. The bins used to estimate the noise floor will also contain the cross- (between PRNs) and auto-correlation power, which are non-zero (Blunt, 2007). Additionally, the true peak of the DDM can appear in-between the measured delay and Doppler bins. This tracking error is estimated to cause up to 1 dB degradation. CYGNSS measurements are also produced at a 1 Hz (or 2 Hz) rate, which means that each DDM contains 1 s (or 0.5 s) of along-track integration time. During this period the specular point moves approximately 6 km (or 3 km) on the Earth's surface, causing the measurements to incur spatial averaging. Finally, the effects of land scattering, vegetation, and any small-scale surface roughness of the inland waters have been neglected in our simulations. All of these effects further degrade the accuracy of the percentage in FFZ footprint approach. After including the effects described above, the retrieval error for the percentage-water-in-footprint algorithm achieves approximately $1\sigma \approx 20\%$ per 1 Hz measurement. Depending on the end-user's application, a new approach to estimating water content may be needed to achieve higher accuracy.

An advantage of GNSS-R over other sensing methods is the large number of measurements that a small constellation of satellites such as CYGNSS produce. We can make use of this property by combining many simulated measurements together to form estimations. One possibility is to average the data into predefined latitude/longitude bins. Using MODIS as the truth dataset for this simulation study and gridding into 0.05 degree bins, we can compare with the map of estimated water for each bin in Fig. 13. First, each SNR measurement is normalized using the procedure described above. Then, the modified SNR values are mapped directly to the corresponding percentage of water given by the area-squared curve (red curve in Fig. 12). Then, these individual estimates are separated into the lat/lon bins based on the reported specular point location and averaged together. Note, these are the estimates formed before introducing measurement model effects into the simulation, thus represent a best-case scenario. The gridded percentage water estimation errors are shown in the bottom plot of Fig. 12. The error variance of the binned estimations decreases compared to the individual measurements (shown in top of Fig. 12) while a bias error mostly persists. The gridded estimations are less noisy than the

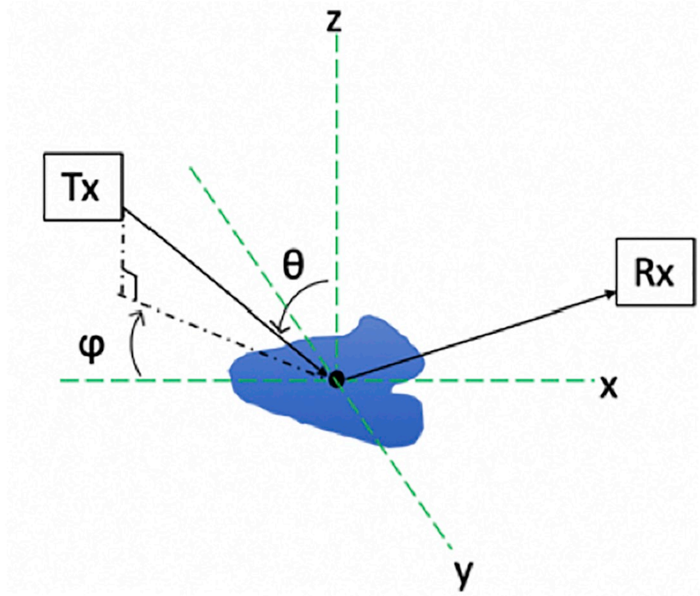

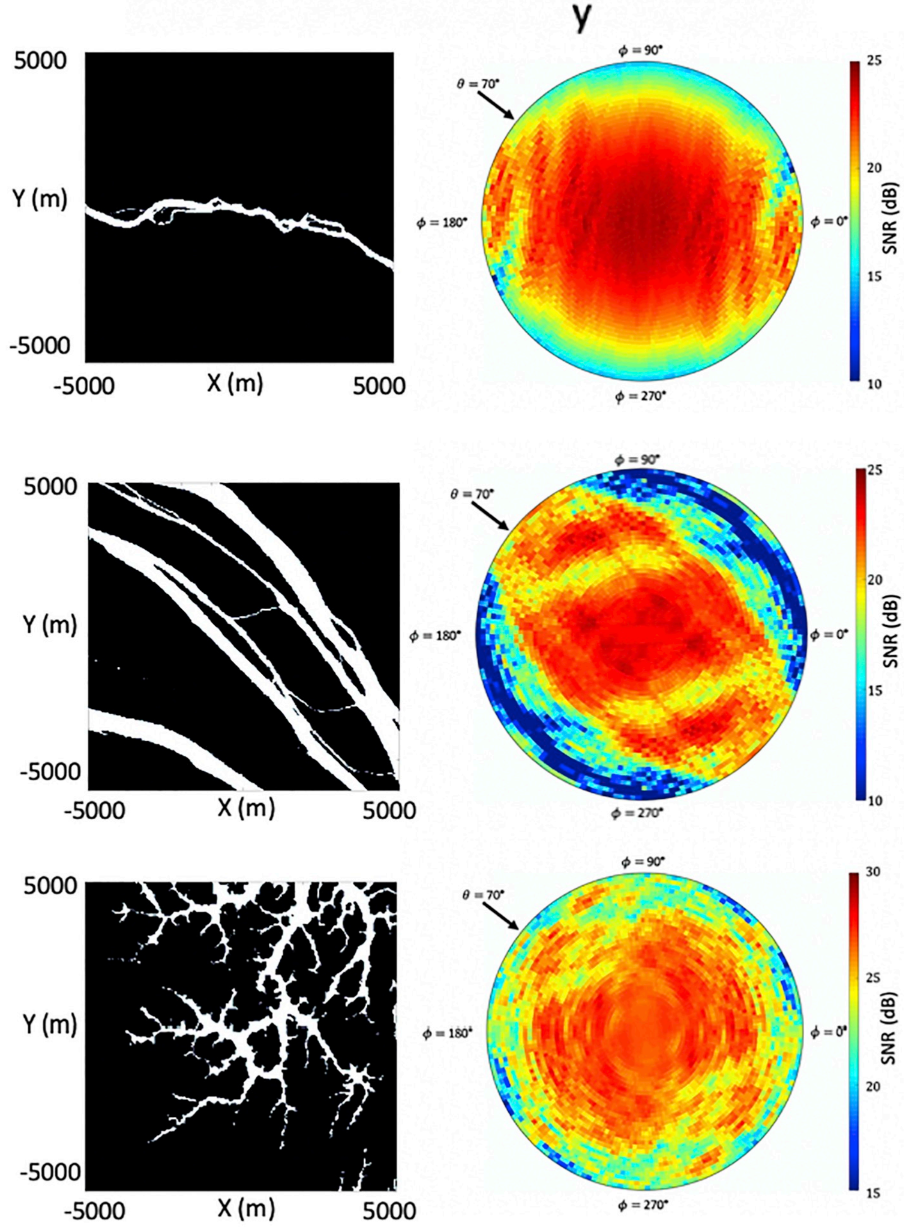

Fig. 9. *Left:* Three example inland water scenes: Aripuana River (top), Soiai River (middle), and Represa de Balbina (bottom). *Right:* Corresponding received peak SNR (dB) as a function of reflection geometry. θ goes from 0 degrees in the center to 70 degrees at the edge of the circle.

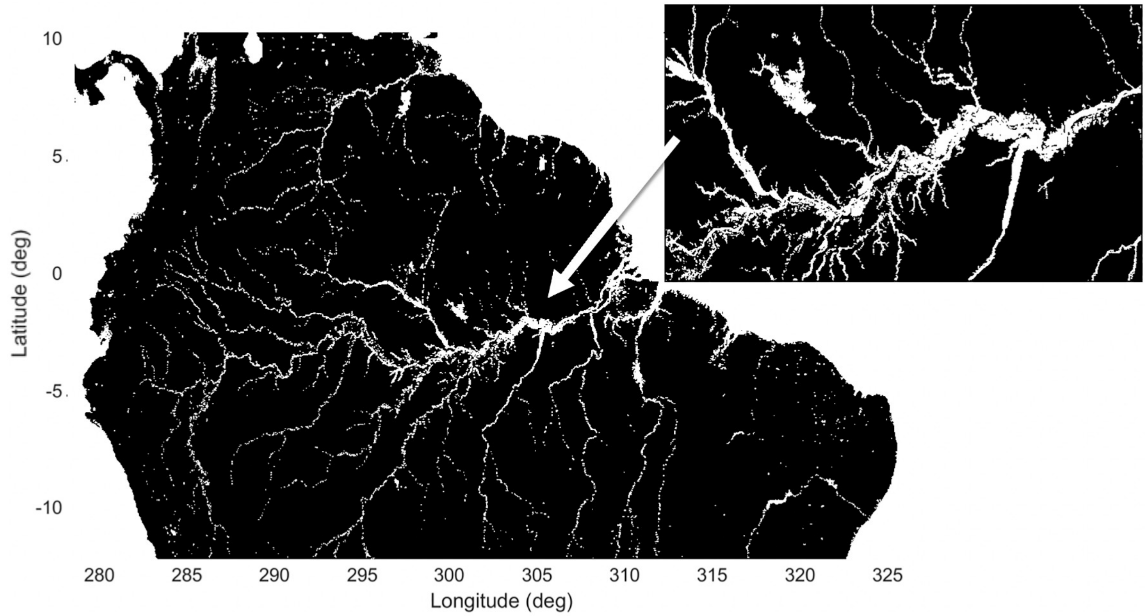

Fig. 10. Amazon River Basin region watermask used for our simulation study. A zoomed in region is shown to highlight the complexity of the watermask.

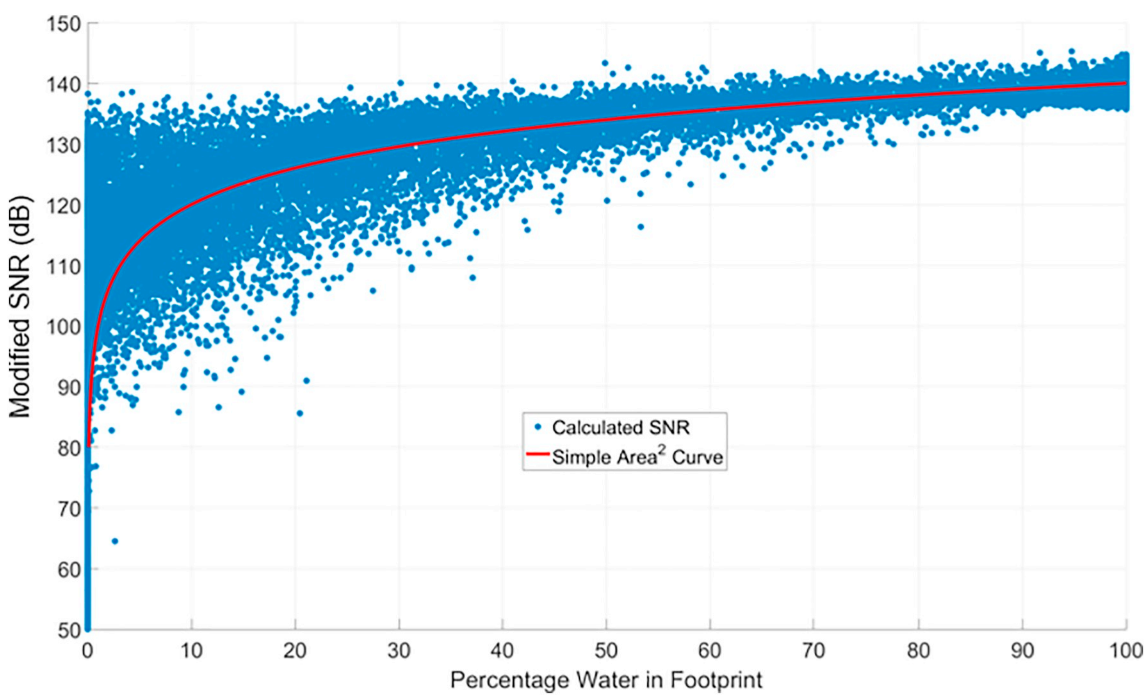

Fig. 11. Modified simulated SNR after normalization for measurement parameters over Amazon region vs. the fraction of water in the first Fresnel zone.

individual measurements, but they still tend to underestimate the true fraction of inland water when there is water in the FFZ, and overestimate the water content when the FFZ is nearly empty.

5. Validation of scattering model using CYGNSS raw IF

In order to validate the accuracy of our scattering model, and thus the fidelity of the simulated retrieval study, we use results calculated with the scattering model to compare with measured CYGNSS data. In addition to its nominal data mode, CYGNSS also has the ability to store the raw samples taken immediately after the ADC at an intermediate frequency for a short duration of time (< 60 s). This is called the raw IF mode. This mode offers much better temporal resolution than the typical 1–2 Hz CYGNSS products, as well as access to the phase information, which is typically lost in the incoherent integration step. We use the raw IF data collected by CYGNSS to examine a representative geophysical scene and compare the results to our forward model.

By using known targets on the surface, we can increase the confidence in our forward model by showing that the simulated results match well with the measurements. The targets were identified by the following properties. First, the target must be an inland body of water that does not exhibit too much surface roughness. This generally limits the targets to be small in size so that large surface waves do not develop. Larger surface waves increase the Rayleigh parameter in (1), and correspondingly increase the decorrelation factor ψ. An increase in ψ then leads to a reduction in the coherent power, and an increase in

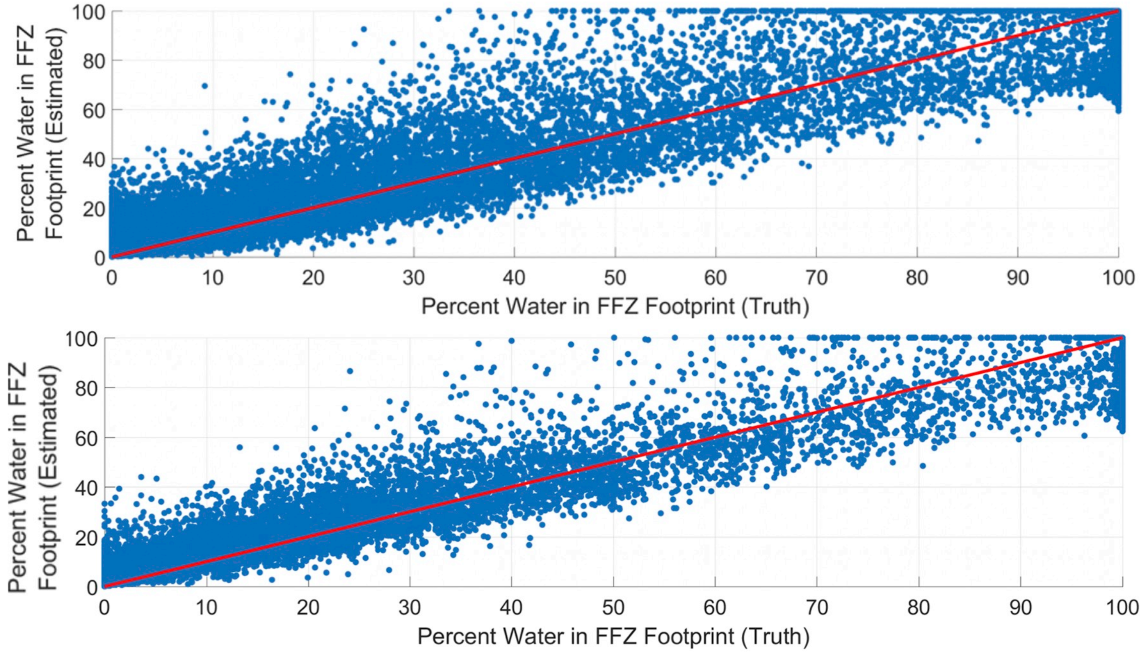

Fig. 12. *Top:* Estimated percentage water vs. truth percentage water in FFZ using simple area-squared approach. Red curve is error free line. *Bottom:* Estimated percentage water vs. truth percentage water after averaging samples in Amazon region into 0.05 degree bins. (For interpretation of the references to colour in this figure legend, the reader is referred to the web version of this article.)

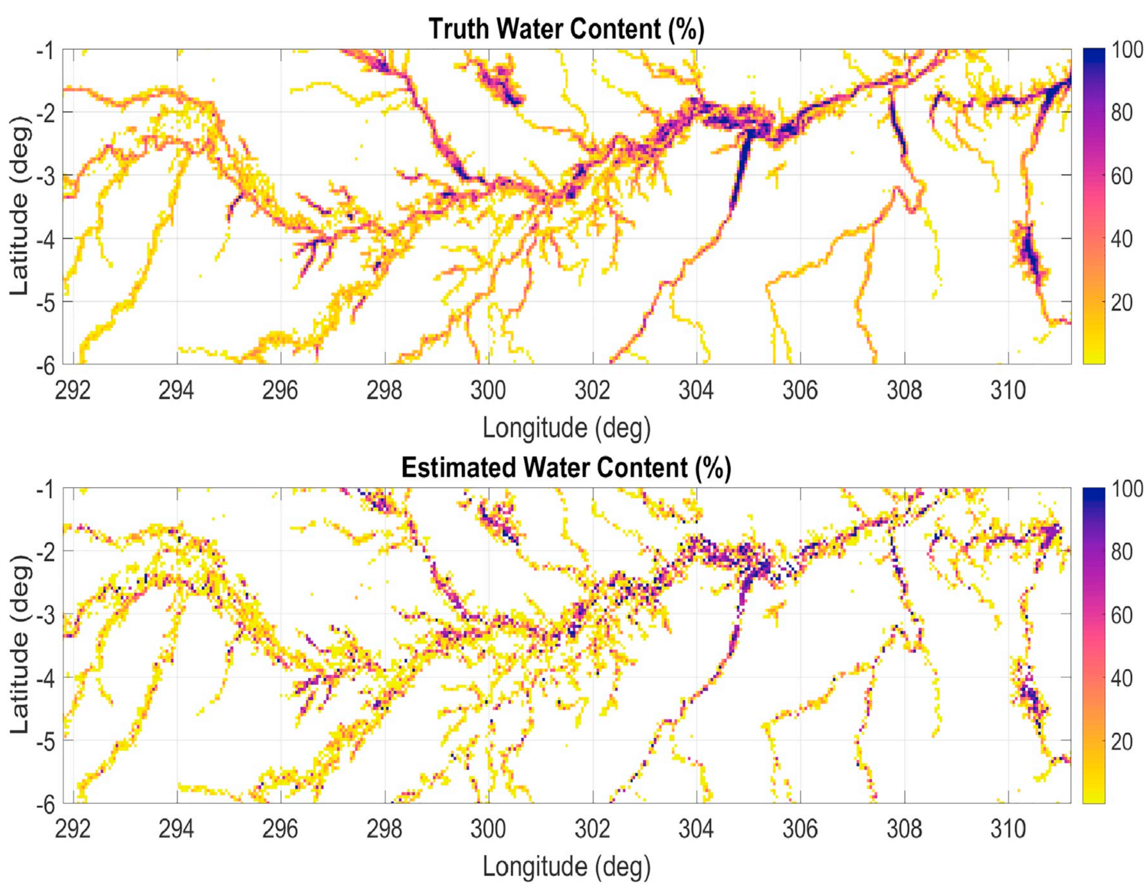

Fig. 13. *Top:* Truth percentage water map close up of Amazon river system averaged into 0.05 degree bins. *Bottom:* Estimated percentage water map for 0.05 degree bins.

diffuse scattering, which is not accounted for in this model. Second, we want the shape and size of the target to be well known. Rapidly changing or unknown targets would be difficult to forward model. Third, it is best for the target to be in an area where the land around it has minimal surface scattering. For example, steep mountain slopes and dry land (with minimal soil moisture) are best. This case best represents

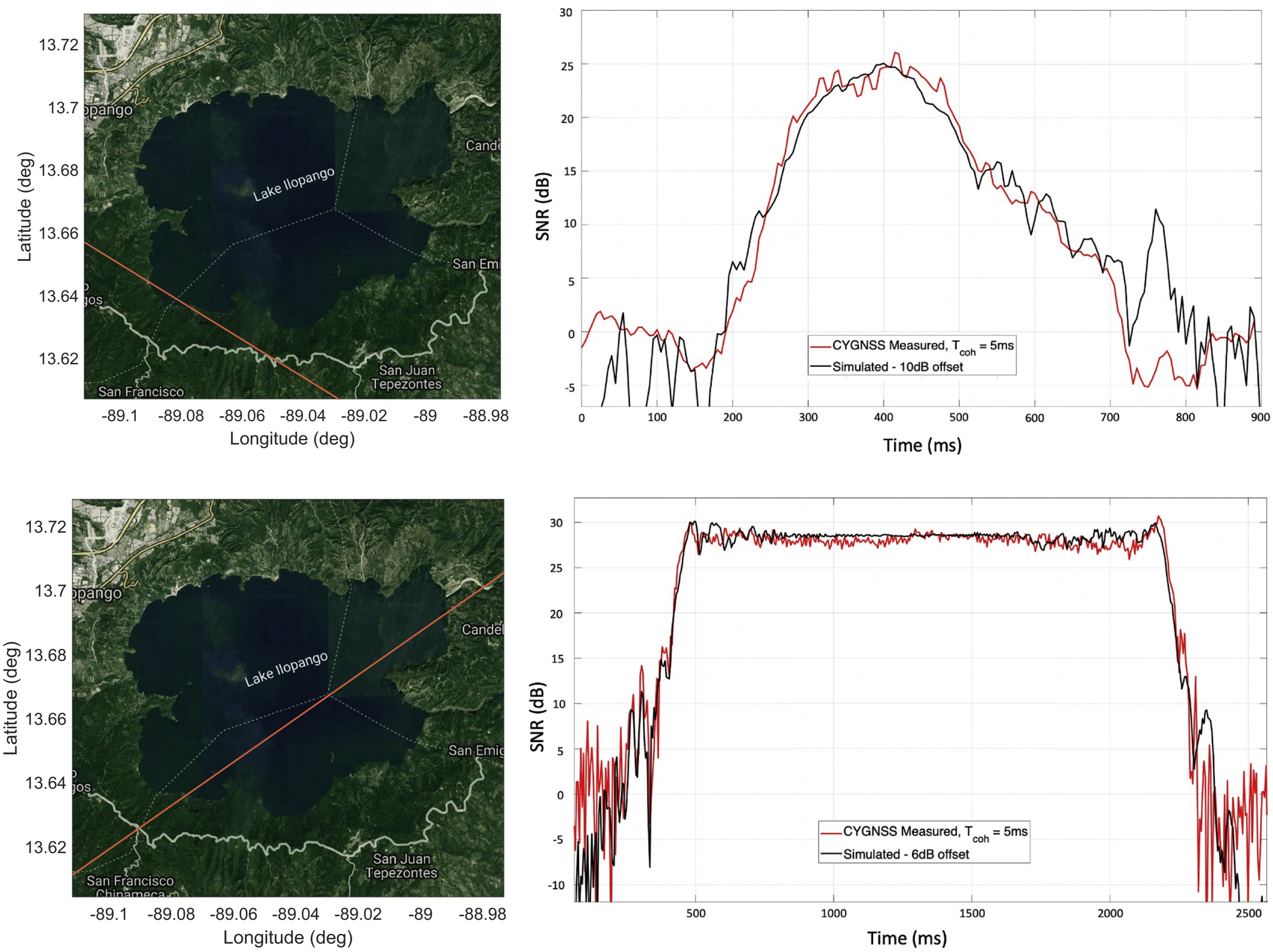

Fig. 14. *Left:* Specular point tracks for two Raw IF recordings over Lake Ilopango (*Top:* Day 229, 2019, *Bottom:* Day 234, 2019). *Right:* Comparison between the measured and simulated peak SNR based on the corresponding specular tracks. Simulated match-up matches the measured power waveforms closely, confirming the accuracy of the scattering model presented in this paper.

the binary water/no water scene that has been simulated. Finally, having open water with no vegetation is necessary as well. Any attenuation due to vegetation would be an additional confounding variable, making the validation difficult. Based on these criteria, we have selected a small crater lake to perform the comparisons with.

Fig. 14 shows maps of target Lake Ilopango with the estimated specular tracks from Raw IF data (left-hand side). At the time of the recording on day 229 of 2019, the winds were approximately 3 km/h NNE with rain. The incidence angle was 36 degrees, and the receiver antenna gain was 8.7 dBi. For the second recording from day 234 of 2019, the winds were 4 km/h SW with rain, and had an incidence angle of 15 degrees with the receiver antenna gain of 7.7 dBi.

The water body was simulated using the coherent scattering model presented in this work. However, for these comparisons, the watermask data was taken from the occurrence values given by the Pekel et al. surface water dataset (Pekel et al., 2016). The raw IF data from the target was processed using a fixed coherent integration time of 5 ms. The increase in T_{coh} over the baseline of 1 ms was chosen to help separate the coherent power from the diffusely scattered power, which provides a more appropriate comparison with simulated coherent power. The corresponding CYGNSS ancillary data for these tracks was run through the updated E2ES with the matching parameters. The local topography was considered when recalculating the specular point track over the lake. The curvature of the Earth was also considered in the position of each piece of the simulation surface grid. Other parameters relating to the simulation (i.e. grid size and resolution) are discussed in Section 2.3. The plots on the right hand side of Fig. 14 show a comparison between the measured and simulated results. It can be seen here that for both tracks, the shape of the simulated data (black) matches well with the measured data (red). Note, there are differences in the absolute magnitude of the receiver SNR. The conversion from simulated power to the predicted SNR used an approximate noise floor power of -140 dBW. This approximation accounts for the portion of the amplitude differences that might come from uncertainties in the true transmitted EIRP, receiver antenna gain, receiver noise power, or other relevant parameters. Further explanation of these differences may also be surface roughness. The small amount of wind and rain reported at the recording times may both have increased the roughness on the surface, leading to several dB attenuation of the signal power. Other parameters have also been ignored in this paper, such as the receiver noise figure (approx. 2 dB), rounding of the cross-correlation amplitude due to limited receiver bandwidth, or the signal quantization loss. Any future work utilizing the precise amplitude of the reflection tracks would greatly benefit from considering these effects.

6. Summary and conclusions

In this paper, we presented the development of a forward model for coherent scattering from inland waters for the purpose of evaluating the accuracy of wetland extent retrieval algorithms applied to CYGNSS data over land. Specifically, we discuss the contributions to the coherent scattering from heterogeneous scenes and find that areas outside the first Fresnel zone contribute to the peak power, and that the peak power of a given scene varies depending on the observation geometry. We have shown that contributions from Fresnel zones beyond the first will affect the total received power, and lead to errors in retrieved water fraction when using a simple percentage-water-in-footprint algorithm. The constructive-destructive nature of varying Fresnel zones leads to ambiguity in the received power when trying to map the received peak power back into a fractional water footprint. In these heterogeneous scenes, often encountered in wetlands and other surface waters, we find that varying factors such as the shape of the scattering surface combined with the Fresnel zone geometry, vegetation attenuation, and small-scale surface roughness can complicate retrievals. Each of these three components can introduce variability in the received power that spans either all or nearly all of the dynamic range of CYGNSS SNR. In order to accurately retrieve one of these three values, the other two should be well characterized.

In this paper, we have also used measured CYGNSS raw IF data to validate the scattering model used in the simulations. The model is capable of reproducing features observed in the measured data. The scattering model presented here will continue to be an asset for the purpose of analyzing errors in current retrieval algorithms as well as future algorithm development, as we can further examine approaches to estimating surface water and wetland extent.

CRediT authorship contribution statement

Eric Loria:Methodology, Software, Validation.**Andrew O'Brien:** Software, Investigation.**Valery Zavorotny:**Methodology, Resources. **Brandi Downs**:Visualization.**Cinzia Zuffada**:Methodology, Supervision, Funding acquisition.

Declaration of competing interest

The authors declare that they have no known competing financial interests or personal relationships that could have appeared to influence the work reported in this paper.

Acknowledgments

This research is funded by NASA ROSES 2017 Project NNH17ZDA001N. The authors would also like to thank the CYGNSS project for providing the Raw IF data in addition to the CYGNSS L1 data provided through PODAAC. Part of the research was carried out at the Jet Propulsion Laboratory, California Institute of Technology, under a contract with the National Aeronautics and Space Administration.

References

Balakhder, A., Al-Khaldi, M., Johnson, J., 2019. On the coherency of ocean and land surface specular scattering for GNSS-R and signals of opportunity systems. IEEE Trans. Geosci. Remote Sens. PP, 1–11. https://doi.org/10.1109/TGRS.2019.2935257.

Bass, F.G., Fuks, I.M., 1979. Wave Scattering from Statistically Rough Surfaces. 93.

Beckmann, P., Spizzichino, A., 1963. The Scattering of Electromagnetic Waves from Rough Surfaces. Macmillan.

Blunt, P., 2007. Advanced global navigation satellite system receiver design. Ph.D. thesis. .

Brivio, P.A., Colombo, R., Maggi, M., Tomasoni, R., 2002. Integration of remote sensing data and GIS for accurate mapping of flooded areas. Int. J. Remote Sens. 23 (3), 429–441. https://doi.org/10.1080/01431160010014729. (Online]. Available: doi:10.1080/01431160010014729).

M. Carroll, C. DiMiceli, M. Wooten, A. Hubbard, R. Sohlberg, J. Townshend, MOD44W MODIS/Terra Land Water Mask Derived from MODIS and SRTM L3 Global 250 m SIN Grid v006, Dataset: NASA EOSDIS Land Processes DAAC. doi:https://doi.org/10.5067/MODIS/MOD44W.006.

Chan, S., Bindlish, R., Hunt, R., Jackson, T., Kimball, J., 2013. Vegetation water content. In: Soil Moisture Active Passive (SMAP), [Online]. Available: https://smap.jpl.nasa.gov/system/internal_resources/details/original/289_047_veg_water.pdf.

Chew, C.C., Shah, R., Zuffada, C., Mannucci, A.J., 2016. Wetland mapping and measurement of flood inundated area using ground-reflected GNSS signals in a bistatic radar system. In: 2016 IEEE International Geoscience and Remote Sensing Symposium (IGARSS), pp. 7184–7187. https://doi.org/10.1109/IGARSS.2016.7730874.

Chew, C., Colliander, A., Shah, R., Zuffada, C., Burgin, M., 2017. The sensitivity of ground-reflected GNSS signals to near-surface soil moisture, as recorded by spaceborne receivers. In: 2017 IEEE International Geoscience and Remote Sensing Symposium (IGARSS), pp. 2661–2663. https://doi.org/10.1109/IGARSS.2017.8127544.

Chew, C., Reager, J., Small, E., 2018. CYGNSS data map flood inundation during the 2017 Atlantic hurricane season. Sci. Rep. 8https://doi.org/10.1038/s41598-018-27673-x. Dec.

Fjørtoft, R., Gaudin, J., Pourthié, N., Lalaurie, J., Mallet, A., Nouvel, J., Martinot-Lagarde, J., Oriot, H., Borderies, P., Ruiz, C., Daniel, S., 2014. KaRIn on SWOT: characteristics of Near-Nadir Ka-Band Interferometric SAR Imagery. IEEE Trans. Geosci. Remote Sens. 52 (4), 2172–2185. Apr. https://doi.org/10.1109/TGRS.2013.2258402.

Fung, A., Eom, H., 1983. Coherent scattering of a spherical wave from an irregular surface. IEEE Trans. Antennas Propag. 31 (1), 68–72. https://doi.org/10.1109/TAP.1983.1142979.

Fung, A.K., Ulaby, F.T., 1978. A scatter model for leafy vegetation. IEEE Trans. Geosci. Electron. 16 (4), 281–286. Oct. https://doi.org/10.1109/TGE.1978.294585.

J. L. Garrison, S. J. Katzberg, M. I. Hill, Effect of sea roughness on bistatically scattered range coded signals from the global positioning system, 1998.

Geremia-Nievinski, F., Silva, M.F.e., Boniface, K., Monico, J.F.G., 2016. GPS diffractive reflectometry: footprint of a coherent radio reflection inferred from the sensitivity kernel of multipath SNR. IEEE Journal of Selected Topics in Applied Earth Observations and Remote Sensing 9 (10), 4884–4891. https://doi.org/10.1109/JSTARS.2016.2579599.

Gleason, S., Hodgart, S., Sun, Yiping, Gommenginger, C., Mackin, S., Adjrad, M., Unwin, M., 2005. Detection and processing of bistatically reflected GPS signals from low earth orbit for the purpose of ocean remote sensing. IEEE Trans. Geosci. Remote Sens. (1558-0644) 43 (6), 1229–1241. https://doi.org/10.1109/TGRS.2005.845643.

Grippa, M., Rouzies, C., Biancamaria, S., Blumstein, D., Cretaux, J., Gal, L., Robert, E., Gosset, M., Kergoat, L., 2019. Potential of SWOT for monitoring water volumes in Sahelian ponds and lakes. IEEE Journal of Selected Topics in Applied Earth Observations and Remote Sensing 12 (7), 2541–2549. Jul. https://doi.org/10.1109/JSTARS.2019.2901434.

Jackson, T., Schmugge, T., 1991. Vegetation effects on the microwave emission of soils. Remote Sens. Environ. (0034-4257) 36 (3), 203–212. https://doi.org/10.1016/0034-4257(91)90057-D. [Online]. Available. http://www.sciencedirect.com/science/article/pii/003442 (579190057D).

Karam, M.A., Fung, A.K., Lang, R.H., Chauhan, N.S., 1992. A microwave scattering model for layered vegetation. IEEE Trans. Geosci. Remote Sens. 30 (4), 767–784. Jul. https://doi.org/10.1109/36.158872.

Kerr, Y.H., Waldteufel, P., Richaume, P., Wigneron, J.P., Ferrazzoli, P., Mahmoodi, A., Al Bitar, A., Cabot, F., Gruhier, C., Juglea, S.E., Leroux, D., Mialon, A., Delwart, S., 2012. The SMOS soil moisture retrieval algorithm. IEEE Trans. Geosci. Remote Sens. 50 (5), 1384–1403. Apr. https://doi.org/10.1109/TGRS.2012.2184548.

Martin-Neira, M., 1993. A Passive Reflectometry and Interferometry System (PARIS): application to ocean altimetry. ESA Journal 17, 331–355.

Morris, M., Chew, C., Reager, J., Shah, R., Zuffada, C., 2019. A novel approach to monitoring wetland dynamics using CYGNSS: Everglades case study. Remote Sens. Environ. 233, 111417. https://doi.org/10.1016/j.rse.2019.111417.

Nghiem, S.V., Zuffada, C., Shah, R., Chew, C., Lowe, S.T., Mannucci, A.J., Cardellach, E., Brakenridge, G.R., Geller, G., Rosenqvist, A., 2017. Wetland monitoring with global navigation satellite system reflectometry. Earth and Space Science 4 (1), 16–39. https://doi.org/10.1002/2016EA000194. [Online]. Available. https://agupubs.onlinelibrary.wiley.com/doi/abs/10.1002/2016EA000194.

Oberstadler, R., Honsch, H., Huth, D., 1997. Assessment of the mapping capabilities of ERS-1 SAR data for flood mapping: a case study in Germany. Hydrol. Process. 11 (10), 1415–1425. https://doi.org/10.1002/(SICI)1099-1085(199708)11:10 < 1415::AID-HYP532 > 3.0.CO;2-2. [Online]. Available. https://onlinelibrary.wiley.com/doi/abs/10.1002/%28SICI%291099-1085%28199708%2911%3A10%3C1415%3A%3AAID-HYP532%3E3.0.CO%3B2-2.

O'Brien, A., 2014. CYGNSS End-to-End Simulator Technical Memo. University of Michigan, Tech. Rep. Space Physics Research Laboratory Doc. 148-0123, pp. 24.

Pavelsky, T.M., Minear, J.T., 2018. How much land surface is under water at any given time? Apr. https://doi.org/10.1029/2018EO104135.

Pekel, J.-F., Cottam, A., Gorelick, N., Belward, A.S., 2016. High-resolution mapping of global surface water and its long-term changes. Nature 540, 418. [Online]. Available:. EP. https://doi.org/10.1038/nature20584.

Ramsar Convention, 2015. Resolution XII.5 (Annex 3). Jun. 2015. [Online] Available. http://www.ramsar.org/sites/default/files/documents/library/cop12_res05_new_strp_e_0.pdf.

Ruf, C., Posselt, D., Majumdar, S., Gleason, S., Clarizia, M., Starkenburg, D., Provost, D., Zavorotny, V., Murray, J., Musko, S., Jelenak, Z., Chang, P., Morris, M., 2016. CYGNSS Handbook. (ISBN: 978-1-60785-380-0).

Saatchi, S.S., Houghton, R.A., Dos Santos Alvala, R.C., Soares, J.V., Yu, Y., 2007. Distribution of aboveground live biomass in the Amazon basin. Glob. Chang. Biol. 13 (4), 816–837. https://doi.org/10.1111/j.1365-2486.2007.01323.x. [Online]. Availbale: https://onlinelibrary.wiley.com/doi/abs/10.1111/j.1365-2486.2007.01323.x.

Thorsos, E.I., 1988. The validity of the Kirchhoff approximation for rough surface scattering using a Gaussian roughness spectrum. The Journal of the Acoustical Society of America 83 (1), 78–92. https://doi.org/10.1121/1.396188. (Online]. Available:

doi:10.1121/1.396188).
Ulaby, F.T., Moore, R.K., Fung, A.K., 1986. Microwave Remote Sensing Active and Passive: From Theory to Applications. 3 Artech House, Inc.
Ulaby, F.T., Haddock, T.H., Kuga, Y., 1990. Measurement and modeling of millimeter-wave scattering from tree foliage. Radio Sci. 25 (3), 193–203. https://doi.org/10.1029/RS025i003p00193. [Online]. Available: https://agupubs.onlinelibrary.wiley.com/doi/abs/10.1029/RS025i003p00193.
Ulaby, F., Long, D., Blackwell, W., Elachi, C., Fung, A., Ruf, C., Sarabandi, K., Zyl, J., Zebker, H., 2014. Microwave Radar and Radiometric Remote Sensing. (ISBN: 978-0-472-11935-6).
Unwin, M., Van Steenwijk, R.d.V., Gommenginger, C., Mitchell, C., Gao, S., 2010. The SGR-ReSI - a new generation of space GNSS receiver for remote sensing. In: Proceedings of the 23rd International Technical Meeting of the Satellite Division of the Institute of Navigation (ION GNSS 2010), pp. 1061–1067.
Voronovich, A.G., Zavorotny, V.U., 2017. The transition from weak to strong diffuse radar bistatic scattering from rough ocean surface. IEEE Trans. Antennas Propag. 65 (11), 6029–6034. Nov. https://doi.org/10.1109/TAP.2017.2752219.
Voronovich, A.G., Zavorotny, V.U., 2018. Bistatic radar equation for signals of opportunity revisited. IEEE Trans. Geosci. Remote Sens. (0196-2892) 56 (4), 1959–1968. https://doi.org/10.1109/TGRS.2017.2771253.
Wang, T., Ruf, C.S., Block, B., McKague, D.S., Gleason, S., 2019. Design and performance of a GPS constellation power monitor system for improved CYGNSS L1B calibration. IEEE Journal of Selected Topics in Applied Earth Observations and Remote Sensing 12 (1), 26–36. Jan. https://doi.org/10.1109/JSTARS.2018.2867773.
Zavorotny, V.U., Voronovich, A.G., 2000. Scattering of GPS signals from the ocean with wind remote sensing application. IEEE Trans. Geosci. Remote Sens. 38 (2), 951–964. Mar. https://doi.org/10.1109/36.841977.
Zavorotny, V., Loria, E., O'Brien, A., Downs, B., Zuffada, C., 2020. Effects of Surface Roughness and Ice on CYGNSS Coherent Scattering from Lakes. (in Preparation).
Zhang, Z., Zimmermann, N.E., Stenke, A., Li, X., Hodson, E.L., Zhu, G., Huang, C., Poulter, B., 2017. Emerging role of wetland methane emissions in driving 21st century climate change. Proc. Natl. Acad. Sci. 114 (36), 9647–9652. https://doi.org/10.1073/pnas.1618765114. ISSN: 0027-8424, eprint:https://www.pnas.org/content/114/36/9647.full.pdf, [Online]. Available: https://www.pnas.org/content/114/36/9647.
Zuffada, C., Chew, C., Nghiem, S.V., Shah, R., Podest, E., Bloom, A.A., Koning, A., Small, E., Schimel, D., Reager, J.T., Mannucci, A., Williamson, W., Cardellach, E., 2016. Advancing wetlands mapping and monitoring with GNSS reflectometry. In: Living Planet Symposium. 740. ser. ESA Special Publication, pp. 83.
Zuffada, C., Chew, C., Nghiem, S.V., 2017. Global Navigation Satellite System Reflectometry (GNSS-R) algorithms for wetland observations. In: 2017 IEEE International Geoscience and Remote Sensing Symposium (IGARSS), pp. 1126–1129. https://doi.org/10.1109/IGARSS.2017.8127155.